An Integrated Inductive Power Transfer System Design With a Variable Inductor for Misalignment Tolerance and Battery Charging Applications

Zhuhaobo Zhang, *Student Member, IEEE*, Fan Zhu, Dehong Xu, *Fellow, IEEE*, Philip T. Krein, *Fellow, IEEE*, and Hao Ma, *Senior Member, IEEE*

***Abstract*—Inductive power transfer (IPT) technology is useful for electric vehicle (EV) charging because of safe, flexible, and convenient features. In this paper, an integrated IPT system design employing variable inductor control is proposed to achieve a target constant current (CC) and constant voltage (CV) battery charging profile with misalignment tolerance. The system is implemented under a fixed switching frequency in both CC and CV modes. Soft switching of the primary inverter can be achieved over the entire charging process and allowed misalignment range without additional switches or dc–dc converters. Theoretical circuit analysis and the system design process are presented. A 3.3-kW prototype is implemented with a 210-mm air gap to demonstrate the validity of the proposed method. Experimental results show that the target CC and CV charging profile can be achieved by adjusting the variable inductor with up to 120 mm of lateral and 300 mm of vertical misalignment. The maximum efficiency of the proposed system is 96.1% at full output power and stays above 95% throughout CC operation.**

***Index Terms*—Constant current/constant voltage charging, inductive power transfer, misalignment tolerance, variable inductor.**

I. Introduction

INDUCTIVE power transfer (IPT) is starting to have commercial impact [1]–[4]. It is relatively safe and flexible, and suitable for electric vehicle (EV) charging. It can be used to make charging convenient.

Lithium batteries for EV charging [5] have high energy density. A two-stage charging strategy that transitions from constant current (CC) to constant voltage (CV), is widely implemented to match battery characteristics [6]. In IPT applications, misalignment can occur because of low positioning precision. Misalignment tends to decrease the coupling coefficient and affects power transmission capability [7]. Various circuit topologies and control strategies have been proposed to deliver the required charging profile given a misalignment range. The methods can be separated into three categories that can be termed "multistage transmission" [8]–[12], "frequency ride-through" [14]–[18] and "compensation switching" [23]–[25].

The multistage transmission method is widely used in IPT systems to match load impedances. The IPT stage can operate under nominal load, and unity power factor is possible. In [8] and [9], additional dc–dc stages are employed to achieve CC and CV operation along with input and output dc voltage regulation. A controller for power regulation is proposed in [10], based on the secondary semiactive rectifiers. Integration of active rectifiers and control strategies, such as phase-shift control and dual-side control, is demonstrated in [11] and [12]. However, the multistage transmission method has disadvantages of high component count, high cost, and high control complexity. The method tends to compromise system efficiency.

A pulse frequency modulation method with fixed duty ratio is employed in [13]. A wide frequency range is required to match varying load impedances. This can increase switching losses. A frequency ride-through method was proposed to charge lithium batteries without additional switches. In [14], two separate frequencies are identified as load-independent current and voltage outputs based on series-series (S-S) compensation. The frequency for current output is used in the CC mode and the frequency for voltage output is used in the CV mode. An IPT system using similar strategies with two intermediate coils to improve coupling was discussed in [15]. The method was developed for series-parallel (S-P) and higher-order compensation topologies in [16]–[18]. However, frequency splitting or bifurcation may occur that influences system stability [19]. The dynamic ride-through process needs to be designed carefully to avoid this.

The compensation switching method combines load-independent CC or CV outputs of fundamental [20] and higher-order compensation topologies [21], [22] to form

Manuscript received October 20, 2019; revised January 10, 2020 and March 2, 2020; accepted March 30, 2020. Date of publication April 15, 2020; date of current version July 20, 2020. This work was supported in part by the National Nature Science Foundation of China under Grant 51577171, and in part by the Zhejiang University/University of Illinois at Urbana–Champaign Institute. Recommended for publication by Associate Editor M. Ponce-Silva. *(Corresponding author: Hao Ma.)*

Zhuhaobo Zhang and Hao Ma are with the College of Electrical Engineering, Zhejiang University, Hangzhou 310027, China, and also with the University of Illinois at Urbana–Champaign Institute, Zhejiang University, Haining 314400, China (e-mail: zzhbpain@163.com; mahao@zju.edu.cn).

Fan Zhu and Dehong Xu are with the College of Electrical Engineering, Zhejiang University, Hangzhou 310027, China (e-mail: zhufanwz@163.com; xdh@zju.edu.cn).

Philip T. Krein is with the College of Electrical Engineering, Zhejiang University, Hangzhou 310027, China, with the University of Illinois at Urbana–Champaign Institute, Zhejiang University, Haining 314400, China, and also with the University of Illinois at Urbana–Champaign, Champaign, IL 61820 USA (e-mail: krein@illinois.edu).

Color versions of one or more of the figures in this article are available online at https://ieeexplore.ieee.org.

Digital Object Identifier 10.1109/TPEL.2020.2987906

hybrid structures with additional ac switches. In [23], switching between hybrid S-S (S-P) and P-S (P-P) topologies is restricted on the primary side. Switching between S-S and S-LCC topologies is implemented on the secondary side in [24]. A hybrid and reconfigurable IPT system is discussed in [25] for a target battery charging profile with high misalignment tolerance. In these IPT converters, ac switches select the modes in the main power path and generate extra conduction losses. They result in a complex system structure that can reduce system efficiency and reliability.

In addition to the three categories, a system using the frequency ride-through method with a semiactive rectifier was proposed in [26]. System efficiency in the CV mode can be improved substantially by employing a novel control strategy. In [27], two different secondary compensation topologies are paralleled on the dc side and the system achieves CC and CV outputs naturally without complex control. In [28], a basic geometric control method is used for seamless CC and CV operation that includes an end charge voltage taper. It adds flexibility for battery charging management and can be adapted for other types of chargers.

The variable inductor control method originates from applications of lighting drivers demonstrated in [29] and [39]–[43]. A low dc bias current is generally used to saturate parts of the magnetic cores. Electrical isolation and safety are maintained because the control windings are decoupled from the main winding. The inductance can be adjusted for various load currents. In IPT applications, a multiply resonant converter is introduced in [30] to compensate misalignment and temperature variations with a variable inductor. It is implemented using mechanical devices. A directional tuning control method is presented in [31] to adjust the inductance on the receiver side. Effects of parameter variations are discussed, but the work does not address high power battery charging. A variable capacitor design is proposed in [32] to adjust the resonant frequency. No active switching is involved and the capacitance can be adjusted continuously compared with conventional switched-mode capacitors. Since the diode and transistor are in parallel with the resonate component, device rating and isolation issues limit the power range of this method.

In this article, an integrated IPT system design employing variable inductance control is proposed for EV charging. The method brings an independent control variable into the system to achieve a target battery charging profile given misalignment. Compared to prior IPT methods, the proposed system design has following advantages. First, it operates at fixed switching frequency. This benefits system reliability and is compatible with standard J2954 [33], in which the recommended nominal frequency is 85 kHz and the range is 79–90.00 kHz for light-duty electric vehicles. Second, a back-end dc–dc stage is eliminated. CC and CV charging modes are achieved with a single IPT stage without additional ac switches. Third, zero voltage switching (ZVS) can be obtained over the entire charging process. Switching losses decrease accordingly. Fourth, battery charging that tolerates misalignment can be achieved.

In this article, impedance analysis of the proposed circuit and characteristics of the CC and CV charging modes are presented in Section II. Detailed design procedures and implementations of the variable inductor are elaborated in Sections III and IV. In Section V, experimental results are obtained from a 3.3 kW prototype to validate the proposed design. Some conclusions are given in Section VI.

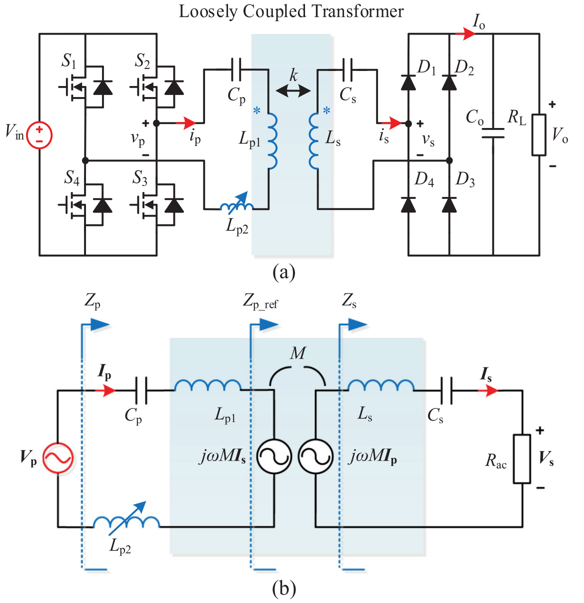

Fig. 1. (a) Proposed circuit topology with a variable inductor. (b) Equivalent mutual inductance circuit model.

II. Circuit Configuration and Characteristics

A. Impedance Analysis of the Proposed Circuit Topology

The proposed circuit topology with a variable inductor is shown in Fig. 1(a). A mutual inductance model is used for the loosely coupled transformer, as represented by the shaded area. The primary circuit consists of a full-bridge inverter and a transmitter coil with *LC* compensation. The inverter is composed of four power MOSFETs (S_1-S_4). The secondary circuit consists of a full-bridge rectifier (diodes D_1-D_4) and a receiver coil with single capacitor compensation. The variable inductor is in series with the primary resonant tank.

The fundamental harmonic approximation (FHA) method is used to analyze the basic characteristics of the proposed circuit topology. The equivalent mutual inductance circuit model is shown in Fig. 1(b). Ignoring high-order harmonics, define

$$\begin{cases} V_p = \frac{4}{\pi}V_{\rm in}, V_s = \frac{4}{\pi}V_o \\ R_{\rm ac} = V_s/\frac{\pi}{2}I_o = \frac{8}{\pi^2}\frac{V_o}{I_o} = \frac{8}{\pi^2}R_L \end{cases} \tag{1}$$

where $V_{\rm in}$ and V_o, respectively, the are system input and output dc voltages. V_p and V_s are magnitudes of the fundamental harmonic voltages after the inverter and before the rectifier, respectively. R_L and $R_{\rm ac}$ are the load and system equivalent load seen after and before the diode rectifier, respectively.

Impedance characteristics can be obtained from loop equations. The corresponding resonant condition is given by

$$\omega = 2\pi f_s = \frac{1}{\sqrt{L_{p1}C_p}} = \frac{1}{\sqrt{L_sC_s}} \tag{2}$$

where ω represents the system frequency in rad/s. The primary and secondary coil inductances L_{p1} and L_s resonate with compensation capacitors C_p and C_s. Z_p, Z_{p_ref}, and Z_s are equivalent impedance variables seen from various terminals of the proposed circuit shown in Fig. 1(b). For the resonant condition, the input magnitude and phase of Z_p are given by

$$\begin{cases} |Z_\mathrm{p}| = \sqrt{(\omega L_{p2})^2 + \frac{(\omega M)^4}{R_{ac}^2}} \\ \mathrm{angle}(Z_\mathrm{p}) = \tan^{-1}\left(\frac{L_{p2}R_\mathrm{ac}}{\omega M^2}\right) \end{cases} \tag{3}$$

where M represents the mutual inductance of the loosely coupled transformer. Primary and secondary resonant currents can be derived, and are given by

$$\begin{cases} \dot{I}_p = \frac{\dot{V}_p}{Z_p} = \frac{\dot{V}_p}{j\omega L_{p2} + \frac{(\omega M)^2}{R_{ac}}} \\ \dot{I}_s = \frac{j\omega M}{Z_s}\dot{I}_p = \frac{j\omega M}{R_{ac}}\dot{I}_p. \end{cases} \tag{4}$$

Conservation of energy requires

$$\mathbf{Re}\{\dot{V}_p \overset{*}{I}_p\} = \mathbf{Re}\left\{\frac{V_p^2}{-j\omega L_{p2} + \frac{(\omega M)^2}{R_\mathrm{ac}}}\right\} = \frac{\left(\frac{V_s}{\sqrt{2}}\right)^2}{R_\mathrm{ac}} = \frac{V_o{}^2}{R_L} \tag{5}$$

in the lossless case. The voltage gain and transconductance characteristics of the proposed circuit are

$$\frac{I_o}{V_\mathrm{in}} = \sqrt{\left(\frac{8}{\pi^2}\right)^2 \frac{k^2 L_s L_{p1}}{L_{p1}^2\omega^2 k^4 L_s^2 + L_{p2}^2\left(\frac{8}{\pi^2}R_L\right)^2}} \tag{6}$$

$$\frac{V_o}{V_\mathrm{in}} = \sqrt{\frac{k^2 L_s L_{p1}\left(\frac{8}{\pi^2}R_L\right)^2}{L_{p1}{}^2\omega^2 k^4 L_s^2 + L_{p2}^2\left(\frac{8}{\pi^2}R_L\right)^2}} \tag{7}$$

where k represents the coupling coefficient of the loosely coupled transformer shown in Fig. 1(a).

Internal resistances of the transmitter and receiver coils influence system output and generate losses. The preceding analysis can be extended to include resistance, except that (5) is not applicable. For the resonant condition, the voltage gain and transconductance characteristics of the circuit are given by where R_p and R_s represent primary and secondary coil resistances.

Conventional S-S compensation acts as a constant current output at resonance [20]. This characteristic can be obtained by setting inductance L_{p2} to zero in (6). In contrast, the proposed circuit controls variable inductance L_{p2} to achieve CC and CV battery charging performance for a fixed switching frequency.

TABLE I
SPECIFICATIONS OF THE IPT BATTERY CHARGER

Parameters	**Symbols**	Values
Power rating	P_o	3.3 [kW]
Input voltage	V_in	400 [V]
Output Voltage	V_out	235-420 [V]
Charging Current	I_o	7.85 [A]
Load impedance	R_L	30-535 [Ω]

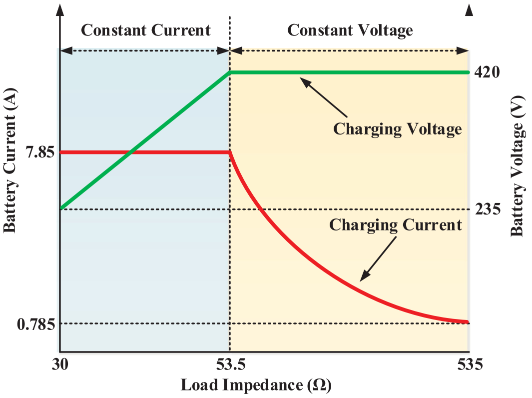

Fig. 2. CC and CV charging profile of EV lithium batteries under 3.3 kW power rating.

B. Implementations of CC/CV Battery Charging With the Proposed IPT System

The specifications of the proposed IPT system are presented in Table I and the target CC and CV charging profile is illustrated in Fig. 2. Initially, the charger delivers rated 7.85 A as the battery voltage increases. The charging power reaches a maximum at the 420 V battery voltage limit. Current tapers during the subsequent CV mode. The process ends when the current drops below 10%. The load impedance rises from 30 to 535 Ω.

The current and voltage operating modes can be achieved by suitably adjusting the variable inductance. The circuit transconductance and voltage gains in (6) and (7) are related to load resistance, coupling coefficient, and variable inductance when primary and secondary coil inductances are fixed. Operating constraints on the variable inductance in the two modes become

$$\mathbf{CC}\colon L_{p2} = \sqrt{\frac{\left(\frac{V_\mathrm{in}}{I_o}\right)^2\left(\frac{8}{\pi^2}\right)^2 k^2 L_{p1}L_s - \omega^2 k^4 L_{p1}^2 L_s^2}{\left(\frac{8}{\pi^2}R_L\right)^2}} \tag{10}$$

$$\mathbf{CV}\colon L_{p2} = \sqrt{\left(\frac{V_\mathrm{in}}{V_o}\right)^2 k^2 L_{p1}L_s - \frac{\omega^2 k^4 L_{p1}^2 L_s^2}{\left(\frac{8}{\pi^2}R_L\right)^2}}. \tag{11}$$

$$\frac{I_o}{V_\mathrm{in}} = \sqrt{\left(\frac{8}{\pi^2}\right)^2 \frac{\omega^2 k^2 L_s L_{p1}}{\omega^2 L_{p2}^2\left(R_s + \frac{8}{\pi^2}R_L\right)^2 + \left[L_{p1}\omega^2 k^2 L_s + R_p\left(R_s + \frac{8}{\pi^2}R_L\right)\right]^2}} \tag{8}$$

$$\frac{V_o}{V_\mathrm{in}} = \sqrt{\frac{\omega^2 k^2 L_s L_{p1}\left(\frac{8}{\pi^2}R_L\right)^2}{\omega^2 L_{p2}^2\left(R_s + \frac{8}{\pi^2}R_L\right)^2 + \left[L_{p1}\omega^2 k^2 L_s + R_p\left(R_s + \frac{8}{\pi^2}R_L\right)\right]^2}} \tag{9}$$

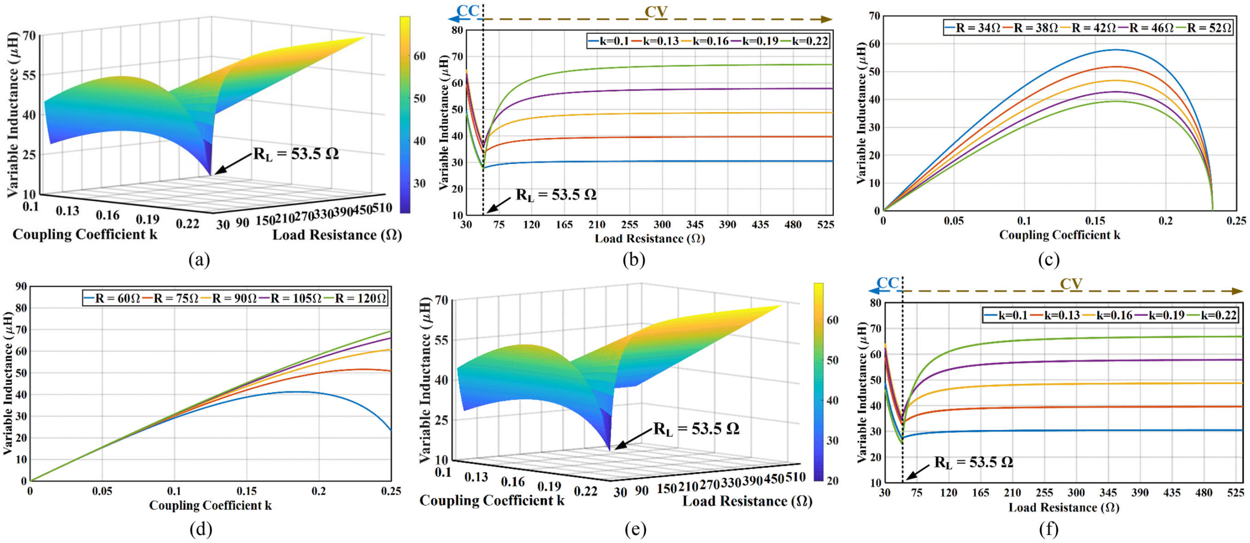

Fig. 3. Constraint curves of the variable inductance for various coupling coefficients and load resistances. (a) In three-dimensional space. (b) Cross-sectional views of various coupling coefficients. (c) Cross-sectional views of various load resistances in the CC mode, and (d) in the CV mode. (e) In three-dimensional space considering coil resistances. (f) Cross-sectional views of various coupling coefficients considering coil resistances.

The corresponding constraint curves are shown in Fig. 3(a)–(d). The system specifications are those in Table I and the transmitter and receiver coil inductances are 330 μH.

Constraint curves of the variable inductance for various coupling coefficients and load resistances are shown in the 3-D plot in Fig. 3(a). The curves behave differently in CC and CV modes. Section views for various coupling coefficients and load resistances are shown in Fig. 3(b)–(d) to illustrate the characteristics more clearly. In Fig. 3(b), constraint curves decrease or increase monotonically for fixed coupling coefficient in the respective CC and CV modes. In CV mode, the target output voltage can be achieved with small adjustment of the variable inductance, especially when load resistance is high. Sensitivity to the inductance value is higher in CC mode. Misalignment characteristics are shown in Fig. 3(c) and (d). The required inductance value is approximately quadratic as coupling changes in CC operation. The behavior is less variable in CV mode. In the system under study, the coupling coefficient is limited by a 210-mm air gap and will not exceed 0.25. The variable inductance can be controlled in terms of constraint curves and CC/CV battery charging can be implemented accordingly.

In accordance with (8) and (9), operating constraints on the variable inductance in CC and CV modes become considering coil resistances. The quality factor of coils generally lies between 100 and 500 in IPT systems for electric vehicle charging applications [34]. Resistances R_p and R_s are both selected as 0.5 Ω for 85 kHz frequency. Corresponding constraint curves of the variable inductance are shown in Fig. 3(e)–(f) to achieve the system specifications. Compared to the lossless case, the maximum deviation of the variable inductance is approximately 1.5%. This deviation can be compensated with a closed-loop control. Consequently, coil resistances have little influence on system design procedures.

C. ZVS Operation of the Proposed IPT System

Characteristic curves of the input impedance, Z_p, are shown in Fig. 4. The curves are plotted in terms of (3) and constraints (10) and (11) using the variable inductor control method. Equation (10) can be simplified as

$$L_{p2}R_L = \sqrt{\frac{\left(\frac{V_{\text{in}}}{I_o}\right)^2\left(\frac{8}{\pi^2}\right)^2 k^2 L_{p1}L_s - \omega^2 k^4 L_{p1}^2 L_s^2}{\left(\frac{8}{\pi^2}\right)^2}}. \tag{14}$$

From (14), in CC mode, the product of variable inductance L_{p2} and load resistance R_L is constant when other parameters are fixed. This results in a constant phase angle for Z_p that can be obtained from (3) for a certain coupling coefficient k. Similarly, (3) and (7) imply a constant magnitude of Z_p in CV mode.

Zero voltage switching on the primary side will help achieve high system efficiency. To obtain ZVS operation, an inductive

$$\textbf{CC}\colon L_{p2} = \sqrt{\frac{\left(\frac{V_{\text{in}}}{I_o}\right)^2\left(\frac{8}{\pi^2}\right)^2\omega^2k^2L_{p1}L_s - \left[R_p\left(R_s+\frac{8}{\pi^2}R_L\right)+\omega^2k^2L_{p1}L_s\right]^2}{\omega^2\left(\frac{8}{\pi^2}R_L+R_s\right)^2}} \tag{12}$$

$$\textbf{CV}\colon L_{p2} = \sqrt{\frac{\left(\frac{V_{\text{in}}}{V_o}\right)^2\left(\frac{8}{\pi^2}R_L\right)^2\omega^2k^2L_{p1}L_s - \left[R_p\left(R_s+\frac{8}{\pi^2}R_L\right)+\omega^2k^2L_{p1}L_s\right]^2}{\omega^2\left(\frac{8}{\pi^2}R_L+R_s\right)^2}} \tag{13}$$

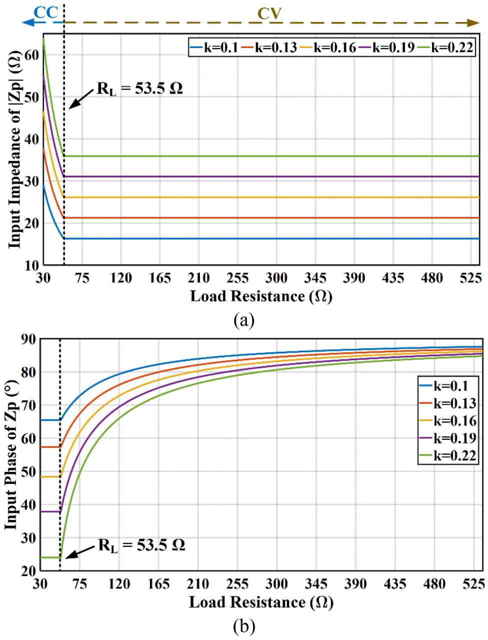

(a)

(b)

Fig. 4. Characteristic curves of the proposed circuit topology for (a) impedance of $|Z_p|$ and (b) phase of Z_p.

input impedance is expected for both CC and CV modes. Conventional S-S compensation adjusts the switching frequency or primary capacitor values slightly to obtain an inductive input impedance. From Fig. 4, Z_p is inductive throughout the defined operating range. In this case, soft switching can be achieved naturally with this variable inductor, an advantage of the proposed system.

The resonant current behavior can be obtained based on Fig. 4. The primary resonant current magnitude gradually increases in CC mode and maintains a maximum value once the circuit enters CV mode. The magnitude of secondary resonant current behaves similarly, but is in quadrature. Both currents rise when the coupling coefficient decreases. The input phase angle behaves differently. It stays constant in CC mode and increases to a large value in CV mode. The phase increases when the misalignment value increases.

Conduction loss is a major issue in an IPT system. The MOSFET ON-state resistances, diode drops, and ac coil resistances contribute. When system parameters are fixed, conduction losses are related to resonant currents. Losses can be relatively low in CC mode because of high input impedance and low phase angle of Z_p. However, loss begins to increase when the charger enters CV mode. High resonant currents result in high reactive power and high conduction losses. Losses also grow with misalignment. System efficiency decreases accordingly. This is a typical challenge in resonant charger designs and implies the need for a suitable active power-off strategy when the batteries reach a target state of charge.

III. DESIGN PROCEDURES AND CONSIDERATIONS

In this section, design procedures and some considerations for the resonant elements and transformer coils are presented, based on a nominal 3.3-kW charger.

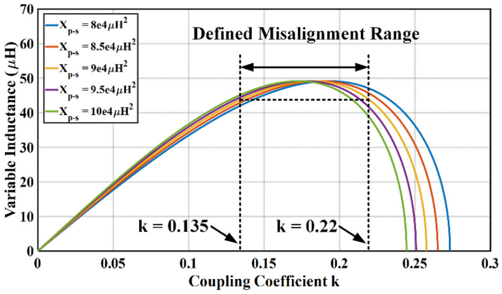

Fig. 5. Constraint curves of the variable inductance in the CC mode with various defined variable X_{p-s}.

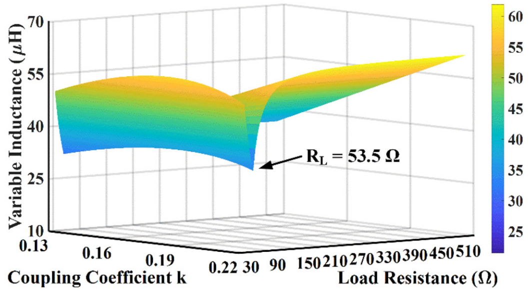

Fig. 6. Constraint curves of the variable inductance in three-dimensional space with optimized parameters.

A. Design of the Variable Inductance Range

Variable inductance is achieved using an independent dc current to change the core incremental permeability. Specific design of the inductor is discussed in Section IV. The range of inductance is limited because of the large air gap in this application. Constraint curves in Fig. 3(a) and (b) show that the minimum and maximum values of the variable inductance in both CC and CV modes are almost equal. The values in CC mode are more sensitive to load change. Therefore, CC mode characteristics are considered to determine the variable inductance range.

Consider a typical load resistance of 40 Ω in CC mode. Define X_{p-s} to be the product $L_{p1}L_s$. Constraint curves are shown in Fig. 5 for various values of X_{p-s}. The variable inductance range can be optimized in terms of the maximum coupling level and the maximum resonant current rating. The former is obtained based on measurements of the transformer while the latter is obtained in terms of the current rating of MOSFET and transformer coils. The limit on misalignment occurs in CV operation at the lowest coupling coefficient. This is where the resonant current magnitude reaches its maximum. The final misalignment range corresponds to a coupling coefficient between 0.135 and 0.22. The value of X_{p-s} can be obtained since L_{p2} has the same value at the range boundaries. By these means, the variable inductance range can be minimized. Constraint curves with optimized parameters are shown in Fig. 6. The value of X_{p-s} is selected to be 88 000 and the range of the variable inductance lies between approximately 31 μH and 62 μH.

B. Design of the Transformer Structure

Loosely coupled transformers with large air gaps are important in an IPT system. IPT transformer pads seek to maximize

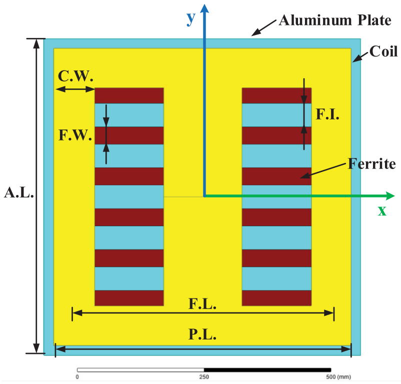

Fig. 7. Employed DD structure for the 3.3-kW IPT battery charger.

TABLE II
SPECIFICATIONS OF THE PAD DIMENSIONS

Parameters	Symbols	Values
Ferrite length	**F.L.**	480 [mm]
Ferrite width	**F.W.**	40 [mm]
Ferrite bars	/	6
Ferrite pieces	/	60*40*10 [mm]
Ferrite interval	**F.I.**	47.5 [mm]
Coil width	**C.W.**	80 [mm]
Pad length	**P.L.**	600 [mm]
Aluminum length	**A.L.**	625 [mm]
Air gap	/	210 [mm]

coupling coefficient k and quality factor Q while minimizing weight and volume.

Several transformer structures were studied in [35] and [36]. The DD type structure is selected here, and is shown in Fig. 7. Dimensions and attributes are listed in Table II. Ferrite bars are used to enhance flux. There are six ferrite bars between the aluminum plate and the coil. The bars are fixed between two epoxy resin boards, with the coils arranged along the surface. Ferrite dimensions and coil width have been optimized with a 3-D finite element modeling (FEM) tool to maximize the coupling coefficient. Simulation results of coupling coefficient k versus axial misalignment are shown in Fig. 8. Coupling characteristics behave differently in lateral (x-axis) and vertical (y-axis) misalignment directions. Vertical misalignment perpendicular to the ferrite bars has less impact than lateral misalignment. The maximum allowed misalignment values in lateral and vertical directions are approximately 130 mm and 310 mm, respectively. The measured coupling coefficients are typically 5-10% lower than in simulation. The allowed misalignment ranges have been reduced by 10% to account for this.

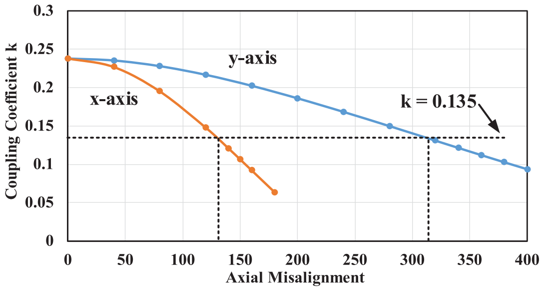

Fig. 8. Simulation results of coupling coefficient characteristics versus axial misalignment.

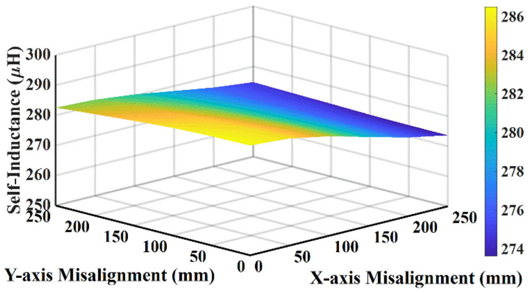

Fig. 9. Simulation results of self-inductance variations versus axial misalignment.

C. Design of the Transmitter and Receiver Coil Inductances

The transmitter and receiver coil inductances are designed based on the above simulation results. The design principles include the following requirements.

1) The number of turns needs to be an integer.
2) The ratio of transmitter and receiver coil inductances needs to match the voltage gain at the nominal operating point.
3) The constraints and simulation results need to be considered.

Self-inductance values were obtained from the FEM simulation with a single-turn coil. Fractional turns are avoided since they could lead to flux imbalance. Coil turns are given by integers N_p and N_s. From Fig. 4, the phase angle on Z_p is relatively small at the nominal operating point. A relationship between the ratio of coil turns and system voltage gain can be obtained in terms of conventional S-S compensation topology guidelines [34]. The proposed system operates under fixed switching frequency. Therefore, design rules to avoid pole splitting or bifurcation are not needed here [19], [34].

Misalignment between transmitter and receiver coils causes variations of the coupling coefficient and self-inductances. Simulation results of the self-inductance L_{p1} versus axial misalignment are shown in Fig. 9. The number of coil turns is selected

$$L_{p2} = \sqrt{\frac{\left(\frac{V_{\text{in}}}{I_o}\right)^2\left(\frac{8}{\pi^2}\right)^2 k^2(L_{p1}-\Delta L_p)(L_s-\Delta L_s) - \omega^2 k^4 (L_{p1}-\Delta L_p)^2(L_s-\Delta L_s)^2}{\left(\frac{8}{\pi^2}R_L\right)^2}} \tag{15}$$

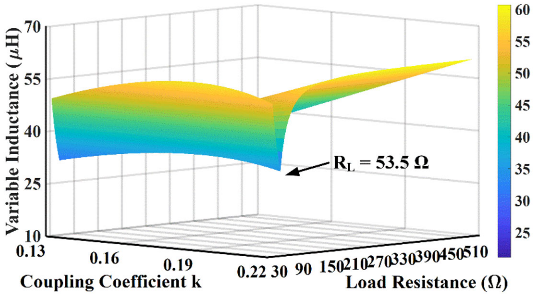

Fig. 10. Constraint curves of the variable inductance in three-dimensional space for the maximum self-inductance variation.

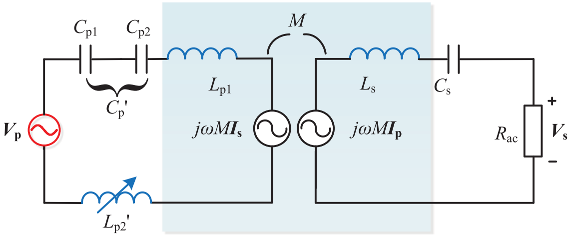

Fig. 11. Proposed circuit topology with optimized resonant condition.

as 11. The maximum variation range is 11.7 μH. This is 4.1% of the nominal value. In this case, the maximum output voltage and current variations are, respectively, 6.76 V and 0.13 A for the nominal load. The results can be calculated from (6) and (7) for a given value of the variable inductance. In practical system operation, variations of self-inductance can be denoted as ΔL_p and ΔL_s. The operating constraint on the variable inductance L_{p2} in CC mode becomes and that in CV mode changes similarly. Corresponding constraint curves are shown in Fig. 10 for the maximum self-inductance variation. Compared to the case with optimized parameters in Fig. 6, the maximum deviation of the variable inductance is approximately 2.7%. This deviation can be compensated with a closed-loop control.

Variation of the self-inductance is usually minor for static electric vehicle charging applications. However, system parameters should be designed carefully for IPT applications with a small air gap, such as rail transportation. The self-inductance variation can be substantial in such cases [37].

D. Considerations About Resonance

The proposed topology provides an alternative method to adjust the inductance range by modifying the resonant condition in (3). As shown in Fig. 11, primary resonant capacitor C_p' can be split into two parts based on the preceding design procedures. Capacitor C_{p1} resonates with coil inductance L_{p1} and C_{p2} compensates part of L_{p2}. The new resonant condition is

$$\begin{cases}\omega = 2\pi f_s = \frac{1}{\sqrt{L_{p1}C_{p1}}} = \frac{1}{\sqrt{L_s C_s}}\\ C'{}_p = \frac{C_{p1}C_{p2}}{C_{p1}+C_{p2}}\\ L'{}_{p2} = L_{p2} + \frac{1}{\omega^2 C_{p2}}\end{cases} \tag{16}$$

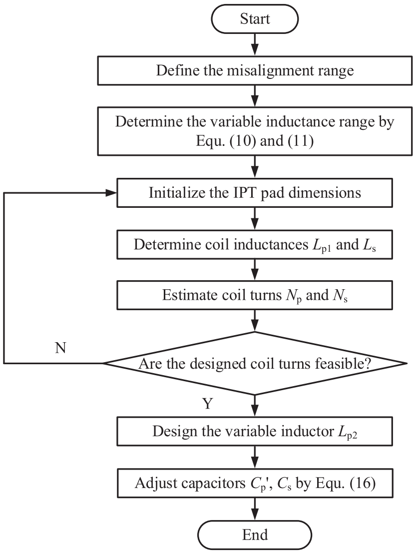

Fig. 12. Design procedures of the proposed IPT system.

where C_p' serves as a capacitor adjustment and L_{p2}' represents the optimized variable inductance.

This method is based on a fixed system operating frequency. It provides a bias to the inductance range which can be larger than the original value. The ratio of the maximum to the minimum inductance decreases. This benefits the variable inductor design. Additionally, the method can compensate the deviations caused by the nonlinearity of the variable inductor.

In practice, the variable inductor can be design first with a smaller air gap. Resonant capacitors C_p' can be selected accordingly. As an alternative method, the addition of capacitor C_{p2} will not affect the previous design procedures and analysis.

In conclusion, the flowchart in Fig. 12 illustrates practical design procedures of the resonant tank for the proposed IPT system. First, the misalignment range is defined. The limit occurs at the lowest coupling coefficient. In this case, the defined variable X_{p-s} and the variable inductance range can be determined based on (10), (11), and specifications in Table I. Next, the IPT pad dimensions are initialized and optimized with a 3D FEM tool to maximize the coupling coefficient. Coil inductances L_{p1}, L_s are determined and coil turns N_p, N_s are estimated in terms of design principles in part *C*. It is necessary to check if the designed coil turns are feasible for the transformer structure. If the results are satisfied, then the variable inductor L_{p2} is designed, as presented in Section IV. Otherwise the pad dimensions need to be adjusted. Finally, capacitors C_p', C_s are adjusted by (16).

IV. IMPLEMENTATION OF VARIABLE INDUCTOR

A variable inductor using EE cores is shown in Fig. 13. The resonant inductor winding N_{ac} is wound on the center leg and two identical control windings N_{dc} are wound on the outer legs. The control windings are connected in series outside the cores and have reversed magnetic flux directions. This structure was

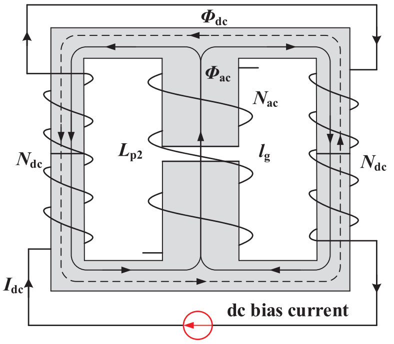

Fig. 13. Variable inductor using EE cores and a dc bias current.

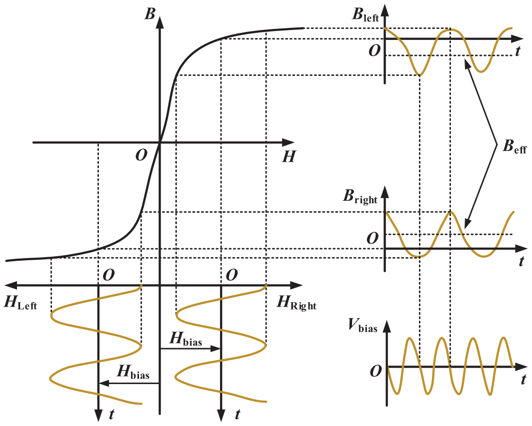

Fig. 14. *B-H* curve and the superimposition results of ac and dc flux that lead to a double frequency V_{bias} voltage.

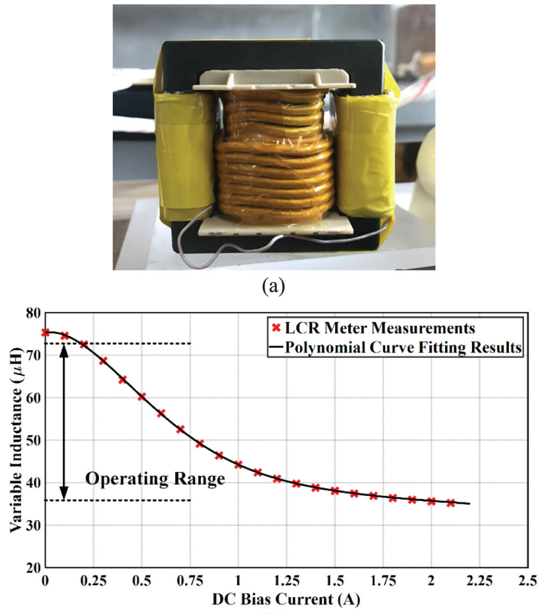

(a)

(b)

Fig. 15. (a) Constructed variable inductor. (b) LCR meter measurements and polynomial curve fitting results of the variable inductor.

TABLE III
VARIABLE INDUCTOR PARAMETERS

Parameters	Symbols	Values
Ferrite material	/	DMR95 (DMEGC)
Ferrite cores	/	EE65
Effective area	A_e	532 [mm^2]
Coil turns of dc bias current	N_{dc}	62
Coil turns of resonant current	N_{ac}	19
Litz wire type of dc bias current	/	40*0.10 [mm]
Litz wire type of resonant current	/	400*0.10 [mm]
Air gap	l_g	6.1 [mm]

discussed in [29] and [38]–[40]. It has the following characteristics.

1) The inductor winding is decoupled from the control windings. Ideally, resonant voltage across the inductor winding will not induce ac voltage in the control windings.
2) The air gap is only in the center leg, minimizing the MMF for control.
3) The ac magnetic flux Φ_{ac} is superimposed on the bias flux Φ_{dc}. As the bias increases, the operating points of both left and right legs on the *B-H* curve move from the linear region to the partial saturation region. The incremental permeability of the outer legs decreases, as does the inductance L_{p2}.

Ideal decoupling between the inductor and control windings is not possible because of the nonlinear *B-H* behavior [41], [42]. In Fig. 14, H_{left} and H_{right} represent magnetic field intensities in the left and right arms. Corresponding magnetic flux densities B_{left} and B_{right} can be obtained in terms of the *B-H* curve. The induced bias voltage V_{bias} is

$$V_{\text{bias}} = V_{\text{left}} - V_{\text{right}} = N_{\text{dc}} \frac{A_e}{2} \frac{d}{dt} (B_{\text{left}} - B_{\text{right}}) \qquad (17)$$

where A_e denotes the effective core area. A sketch of V_{bias} is shown in Fig. 14. Its frequency is double that of the resonant tank. Effective flux density B_{eff} in left and right arms is lower than when the ac flux is zero. Residual coupling results in higher dc bias current for a given inductance. A precise analytical solution of V_{bias} is difficult because of the nonlinear characteristics. SPICE modeling is used in [41], [43], and [44] to give an approximate design. In practice, the variable inductor is controlled within a feedback loop. CC and CV modes are determined based on output current and voltage samples. A buck converter is implemented to supply the dc bias current and the variable inductance can be controlled indirectly to yield the target output.

For the variable inductor, ferrite is a suitable choice at the target frequency. Here, extra space must be provided for the control windings. A flux limit of 0.1 T will be used in this design to reduce the impact of residual coupling. The volume of inductor increases accordingly. The resonant condition (16) provides a method to adjust the variable inductance range and guides the inductor design. Fig. 15(a) shows the variable inductor. Parameters are listed in Table III. Litz wire was employed. There is no available bobbin for the control windings, so two hand-made supports were fabricated. Polyimide tape was used for insulation.

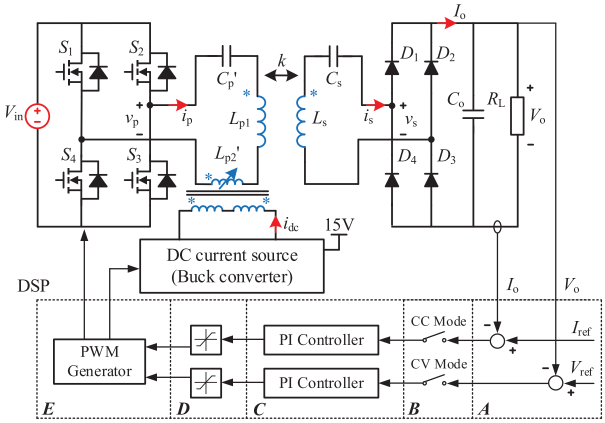

Fig. 16. Closed-loop control structure of the proposed IPT system and implementation of the dc bias current.

Characteristics of the variable inductor were measured using a TH2817 LCR Meter. Measurements and polynomial curve fits are shown in Fig. 15(b). The maximum inductance under zero bias current is about 75.3 μH. Because of residual coupling, the practical operating inductance range will be larger than that derived in Section III. A variation of approximately 10%–20% is reasonable up to 0.1 T. The range is indicated in Fig. 15(b). The maximum dc bias current is less than 2 A and can be reduced with a higher turns count. The actual variable inductance value can be estimated by measuring the dc bias current. A polynomial curve fit for variable inductance L_{p2} vs. dc current $I_{\rm dc}$ gives

$$L_{p2} = 8.422 I_{\rm dc}^5 - 53.9 I_{\rm dc}^4 + 123.4 I_{\rm dc}^3 - 107.7 I_{\rm dc}^2 - 2.052 I_{\rm dc} + 75.94. \tag{18}$$

The curve fit is obtained by the *cftool* toolbox integrated in MATLAB software. The R-square value of the fit is 0.9998.

Closed-loop control is necessary to meet CC and CV mode charging requirements. It can be implemented by adjusting the variable inductance in real time to track the expected charging profile. The closed-loop control structure of the proposed IPT system is shown in Fig. 16 and the flow chart of the control approach is shown in Fig. 17. The controller is implemented in a DSP, and is composed of parts *A*–*E* that represent error generation, mode selection, a PI controller, a PI limiter, and gate signal generation, respectively. Circuit output dc voltage and current are sampled to compensate for transformer misalignment and load variations. When the output voltage V_o is lower than $V_{\rm ref}$ (set to 420 V here), the CC mode PI controller and limiter are activated. Duty ratio of the low-voltage buck converter can be calculated. The $I_{\rm dc}$ output and variable inductance can be adjusted accordingly. Once the output voltage V_o reaches $V_{\rm ref}$, the system switches automatically to CV mode with a PI controller. Gate signals of the primary inverter are not included in the control loop. They operate at a fixed frequency with nearly 50% duty ratio. In practical system operation, primary resonate current protection is necessary to deal with excessive misalignment. The system is activated only when the misalignment lies within the design limits.

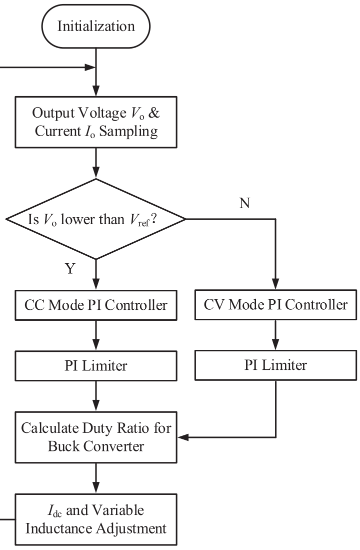

Fig. 17. Flow chart of the closed-loop control scheme.

TABLE IV
MEASURED RESONANT TANK PARAMETERS

Parameters	Symbols	Values
Transmitter coil turns	N_p	11
Transmitter coil inductance	L_{p1}	278.5 [μH]
Transmitter coil ac resistance	R_p	0.31 [Ω]
Receiver coil turns	N_s	12
Receiver coil inductance	L_s	317.3 [μH]
Receiver coil ac resistance	R_s	0.36 [Ω]
Variable inductance	L_{p2}'	75.32 [μH]
Primary resonant capacitor	C_p	11.85 [nF]
Secondary resonant capacitor	C_s	11 [nF]
Resonant frequency	f_s	85 [kHz]

Compared to variable inductor applications in lighting drivers in [29] and [39]–[44], the proposed circuit with magnetic control has following four advantages. First, the proposed IPT system is suitable for high power lithium battery charging applications. The equivalent load impedance and coupling coefficient vary over a wide range. The peak resonant current reaches 20 A at maximum allowed misalignment. Second, a low-voltage converter can provide the dc bias current and this control power is low. Third, sensing of output dc voltage and current for magnetic control is simple to implement. Fourth, as shown in Fig. 15, a 2:1 variable inductance range gives excellent results for CC/CV battery charging performance within a given misalignment range.

V. EXPERIMENTAL RESULTS

A 3.3-kW prototype IPT charging system was built and tested to demonstrate the feasibility of the proposed design. The transformer matches dimensions in Table II and measured parameters of components are listed in Table IV. The variable inductance value is given for zero dc bias current. A picture of the experimental prototype is shown in Fig. 18. The IPT system consists of an H-bridge inverter, the primary and secondary DD structure pads with their compensation capacitors, a variable

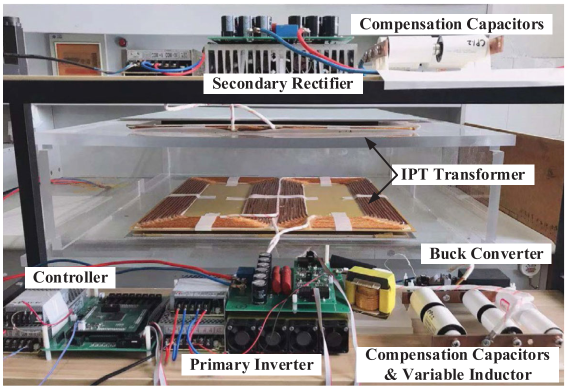

Fig. 18. 3.3-kW IPT experimental prototype.

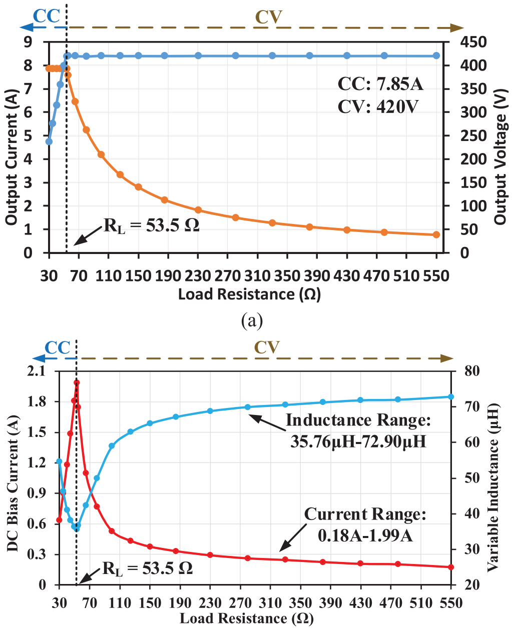

(a)

(b)

Fig. 19. Experimental results of (a) CC/CV charging profile and (b) the dc bias current characteristics and calculated variable inductance values without misalignment.

inductor, a diode rectifier, and load resistances. A Chroma dc source (62100H-450) provides the input power. A SiC MOSFET module (SK45MH120TSCp) from Semikron is used for the full-bridge inverter and four SiC schottky diodes (FFSH2065BDN) are used for the rectifier. Polypropylene film capacitors are used and required compensation capacitances are obtained with series and parallel combinations. Fiberglass sleeves are used to provide adequate insulation strength. The controller is implemented with a Texas Instruments TMS320F28335 DSP to generate switching signals for the inverter and low-voltage buck converter. The operating frequencies are set to 85 and 150 kHz, respectively. The buck converter provides dc bias current for the variable inductor. This bias converter supplies less than 5 W, not included in measurements of system efficiency.

Fig. 19 shows experimental results for a CC and CV charging profile without misalignment. The dc bias currents and calculated variable inductance values are also shown. Load resistances are used to emulate lithium battery charging. The charging currents and voltages track the expected charging profile. The maximum bias current is 1.99 A and the corresponding minimum inductance value is 35.8 μH at the nominal operating condition. Comparing the curve with the theoretical inductance curve shown in Fig. 6, the maximum deviation is approximately 16.5%.

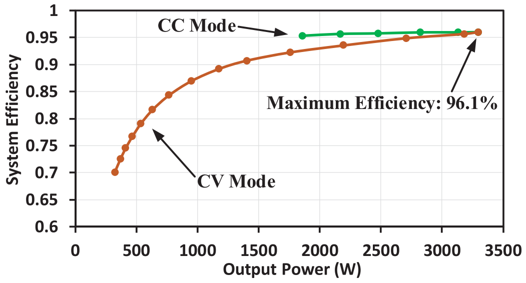

Fig. 20. Experimental results of dc–dc efficiency in the CC and CV modes without misalignment.

Fig. 20 shows experimental results of dc–dc conversion efficiency in CC and CV modes without misalignment. The maximum efficiency is 96.1% at full output power and stays above 95% over the entire CC mode. It is beneficial to maintain high efficiency in CC mode because most battery energy is supplied in this mode [6]. The system efficiency gradually decreases in the CV mode as transmission power decreases. It is less than 85% when the charging power falls below 800 W. This is because the primary resonant current magnitude is almost constant in CV mode. Charging current values can be altered by adjusting the duty ratio of the primary inverter.

The relatively low battery charging efficiency at light load conditions is not unique to the proposed approach. However, in practice a relatively small fraction of total charging energy is delivered near the end of CV mode. Typically, a lithium battery charging system operates above 20% rated charge during almost all of the energy delivery interval. This benefits the battery cycle life. In practice, it is important to prepare an active "no power" operation mode for light load conditions near the end of CV mode [6], [45], [46].

Fig. 21 shows experimental waveforms of the proposed IPT system when the load resistance is 53.5, 40, 30, and 125 Ω, respectively. v_{gs} and v_{ds} are waveforms of one MOSEFT in the full-bridge inverter. i_p and $I_{\rm dc}$ represent the resonant current and dc bias current, respectively. Soft switching conditions are met. The ripple on the dc bias current is double the switching frequency of the resonant current, as expected. From Fig. 4(b), the phase angle of Z_p reaches the minimum in CC mode without misalignment. This is the boundary of system ZVS operation. The phase angle increases as the coupling coefficient decreases and is larger in CV mode. Experimental waveforms in Fig. 21(a)–(c) show ZVS operation for various load resistances in CC mode without misalignment. A larger input phase angle, such as the waveforms in Fig. 21(d) and Fig. 24(a)–(b), makes ZVS operation easier. The results verify that ZVS can be achieved over the entire charging process range.

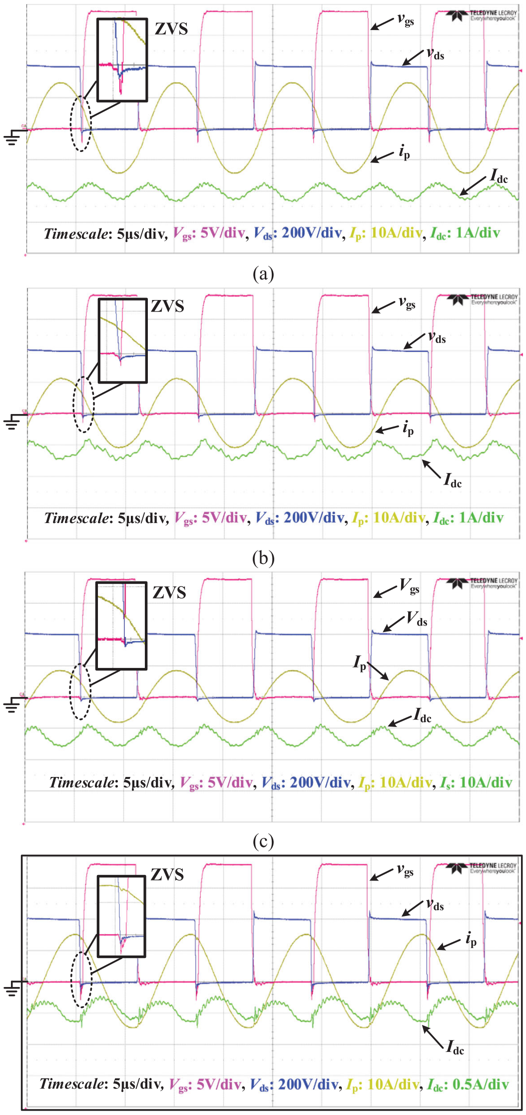

(a)

(b)

(c)

(d)

Fig. 21. Experimental waveforms of the proposed IPT system (a) at nominal operating point ($R_L = 53.5\ \Omega$), (b) in CC mode ($R_L = 40\ \Omega$), (c) in CC mode ($R_L = 30\ \Omega$), and (d) in CV mode ($R_L = 125\ \Omega$).

The measured coupling coefficient without misalignment is 0.221 and the lowest value is 0.135 at 120 mm lateral and 300 mm vertical misalignment. For the misaligned case, load resistances are set to 40 and 125 Ω in the respective CC and CV modes. Experimental results of the variable inductance as a function of dc bias current are shown in Fig. 22.

Fig. 23 shows experimental results of conversion efficiency in CC and CV modes for the maximum misalignment condition. In CC mode, the charging power is 2456 W. In CV mode, it is 1411 W. Primary and secondary resonant currents increase as the coupling coefficient decreases. The system efficiency decreases accordingly.

Fig. 24 shows experimental waveforms of the proposed IPT system when the load resistances are 40 and 125 Ω in the misalignment case with a coupling coefficient of 0.16. Soft switching is still obtained but the resonant current is high.

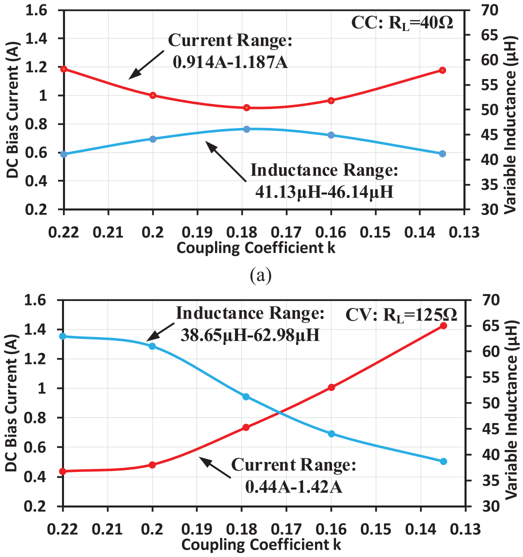

(a)

(b)

Fig. 22. Experimental results of the dc bias current characteristics and calculated variable inductance values under misalignment condition (a) in CC mode ($R_L = 40\ \Omega$), and (b) in CV mode ($R_L = 125\ \Omega$).

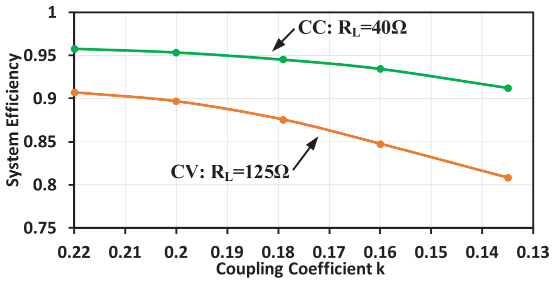

Fig. 23. Experimental results of dc–dc efficiency in the CC and CV modes under misalignment condition.

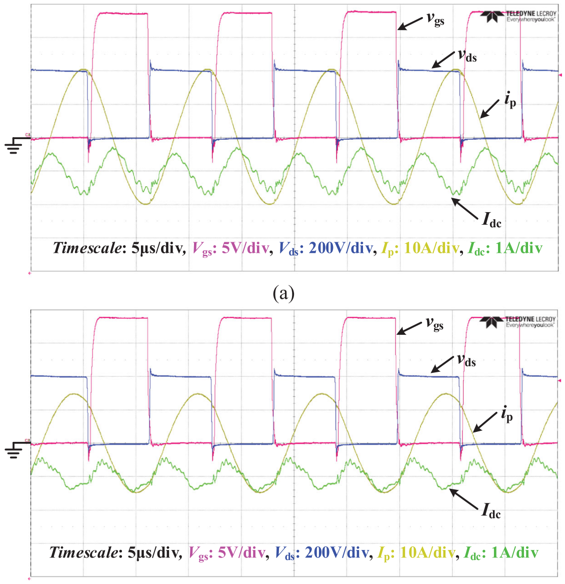

(a)

(b)

Fig. 24. Experimental waveforms of the proposed IPT system under misalignment condition ($k = 0.16$) (a) in CC mode ($R_L = 40\ \Omega$), and (b) in CV mode ($R_L = 125\ \Omega$).

VI. CONCLUSION

In this article, an integrated IPT system design employing a current-controlled variable inductor is proposed to achieve CC and CV lithium battery charging with misalignment tolerance. A 3.3-kW prototype demonstrated its feasibility and validity. The system is implemented under a fixed switching frequency and ZVS can be achieved over the entire charging process and allowed misalignment range. The charging profile can be achieved with up to 120 mm of lateral and 300 mm of vertical misalignment by adjusting the variable inductor. Peak efficiency is 96.1% at full power with a 210-mm air gap. Efficiency stays above 95% over the entire CC mode.

ACKNOWLEDGMENT

The work in this article was led by Principal Supervisors H.Ma, D. Xu, and P. Krein.

REFERENCES

[1] S. Li and C. C. Mi, “Wireless power transfer for electric vehicle applications,” *IEEE J. Emerg. Sel. Topics Power Electron.*, vol. 3, no. 1, pp. 4–17, Mar. 2015.

[2] G. A. Covic and J. T. Boys, “Inductive power transfer,” *Proc. IEEE*, vol. 101, no. 6, pp. 1276–1289, Jun. 2013.

[3] S. Hui, W. Zhong, and C. Lee, “A critical review of recent progress in mid-range wireless power transfer,” *IEEE Trans. Power Electron.*, vol. 29, no. 9, pp. 4500–4511, Sep. 2014.

[4] J. M. Miller, P. T. Jones, J. M. Li, and O. C. Onar, “ORNL experience and challenges facing dynamic wireless power charging of EV’s,” *IEEE Circuits Syst. Mag.*, vol. 15, no. 2, pp. 40–53, Apr.–Jun. 2015.

[5] S. J. Gerssen-Gondelach and A. P. C. Faaij, “Performance of batteries for electric vehicles on short and longer term,” *J. Power Sources*, vol. 212, pp. 111–129, Aug. 2012.

[6] D. Andrea, *Battery Management Systems for Large Lithium-Ion Battery Packs*, 1st ed., Boston, MA, USA: Artech House, 2010.

[7] C. S. Wang, O. H. Stielau, and G. A. Covic, “Design considerations for a contactless electric vehicle battery charger,” *IEEE Trans. Ind. Electron.*, vol. 52, no. 5, pp. 1308–1314, Oct. 2005.

[8] R. Bosshard, J. W. Kolar, and B. Wunsch, “Control method for inductive power transfer with high partial-load efficiency and resonance tracking,” in *Proc. IEEE Int. Power Electron. Conf.*, May 2014, pp. 2167–2174.

[9] M. Kim, D. Joo, and B. K. Lee, “Design and control of inductively power transfer system for electric vehicles considering wide variation of output voltage and coupling coefficient,” *IEEE Trans. Power Electron.*, vol. 34, no. 2, pp. 1197–1208, Feb. 2019.

[10] C. Y. Huang, J. T. Boys, and G. A. Covic, “LCL pickup circulating current controller for inductive power transfer systems,” *IEEE Trans. Power Electron.*, vol. 28, no. 4, pp. 2081–2093, Apr. 2013.

[11] T. Diekhans and R. De Doncker, “A dual-side controlled inductive power transfer system optimized for large coupling factor variations and partial load,” *IEEE Trans. Power Electron.*, vol. 30, no. 11, pp. 6320–6328, Nov. 2015.

[12] K. Colak, E. Asa, M. Bojarski, D. Czarkowski, and O. C. Onar, “A novel phase-shift control of semibridgeless active rectifier for wireless power transfer,” *IEEE Trans. Power Electron.*, vol. 30, no. 11, pp. 6288–6297, Nov. 2015.

[13] C. Zheng *et al.*, “High-efficiency contactless power transfer system for electric vehicle battery charging application,” *IEEE J. Emerg. Sel. Topics Power Electron.*, vol. 3, no. 1, pp. 65–74, Mar. 2015.

[14] Z. Huang, S. Wong, and C. K. Tse, “Design of a single-stage inductive-power-transfer converter for efficient EV battery charging,” *IEEE Trans. Veh. Technol.*, vol. 66, no. 7, pp. 5808–5821, Jul. 2017.

[15] D. H. Tran, V. B. Vu, and W. Choi, “Design of a high efficiency wireless power transfer system with intermediate coils for the on-board chargers of electric vehicles,” *IEEE Trans. Power Electron.*, vol. 33, no. 1, pp. 175–187, Jan. 2018.

[16] X. Qu, H. Chu, S. Wong, and C. K. Tse, “An IPT battery charger with near unity power factor and load-independent constant output combating design constraints of input voltage and transformer parameters,” *IEEE Trans. Power Electron.*, vol. 34, no. 8, pp. 7719–7727, Aug. 2019.

[17] V. B. Vu, D. H. Tran, and W. Choi, “Implementation of the constant current and constant voltage charge of inductive power transfer systems with the double-sided LCC compensation topology for electric vehicle battery charge applications,” *IEEE Trans. Power Electron.*, vol. 33, no. 9, pp. 7398–7410, Sep. 2018.

[18] K. Song, Z. Li, J. Jiang, and C. Zhu, “Constant current/voltage charging operation for series–series and series–parallel compensated wireless power transfer systems employing primary-side controller,” *IEEE Trans. Power Electron.*, vol. 33, no. 9, pp. 8065–8080, Sep. 2018.

[19] C. S. Wang, G. A. Covic, and O. H. Stielau, “Power transfer capability and bifurcation phenomena of loosely coupled inductive power transfer systems,” *IEEE Trans. Ind. Electron.*, vol. 51, no. 1, pp. 148–157, Feb. 2004.

[20] Y. H. Sohn, B. H. Choi, E. S. Lee, G. C. Lim, G. Cho, and C. T. Rim, “General unified analyses of two-capacitor inductive power transfer systems: Equivalence of current-source SS and SP compensations,” *IEEE Trans. Power Electron.*, vol. 30, no. 11, pp. 6030–6045, Nov. 2015.

[21] X. Qu, Y. Jing, H. Han, S. Wong, and C. K. Tse, “Higher order compensation for inductive-power-transfer converters with constant-voltage or constant current output combating transformer parameter constraints,” *IEEE Trans. Power Electron.*, vol. 32, no. 1, pp. 394–405, Jan. 2017.

[22] W. Zhang and C. C. Mi, “Compensation topologies of high-power wireless power transfer systems,” *IEEE Trans. Veh. Technol.*, vol. 65, no. 6, pp. 4768–4778, Jun. 2016.

[23] X. Qu, H. Han, S. Wong, C. K. Tse, and W. Chen, “Hybrid IPT topologies with constant current or constant voltage output for battery charging applications,” *IEEE Trans. Power Electron.*, vol. 30, no. 11, pp. 6329–6337, Nov. 2015.

[24] R. Mai, Y. Chen, Y. Li, Y. Zhang, G. Cao, and Z. He, “Inductive power transfer for massive electric bicycles charging based on hybrid topology switching with a single inverter,” *IEEE Trans. Power Electron.*, vol. 32, no. 8, pp. 5897–5906, Aug. 2017.

[25] Y. Chen, B. Yang, Z. H. Kou, Z. He, G. Cao, and R. Mai, “Hybrid and reconfigurable IPT systems with high-misalignment tolerance for constant current and constant voltage battery charging,” *IEEE Trans. Power Electron.*, vol. 33, no. 10, pp. 8259–8269, Oct. 2018.

[26] Z. Huang, S. Wong, and C. K. Tse, “An inductive-power-transfer converter with high efficiency throughout battery-charging process,” *IEEE Trans. Power Electron.*, vol. 34, no. 10, pp. 10245–10255, Oct. 2019.

[27] P. Cao *et al.*, “An IPT system with constant current and constant voltage output features for EV charging,” in *Proc. IEEE Ind. Electron. Soc. Conf.*, Oct. 2018, pp. 4775–4780.

[28] P. T. Krein, *Elements of Power Electronics*, 2nd ed., New York, NY, USA: Oxford, 2015, pp. 738–739.

[29] M. S. Perdigão, M. F. Menke, Á. R. Seidel, R. A. Pinto, and J. M. Alonso, “A review on variable inductors and variable transformers: Applications to lighting drivers,” *IEEE Trans. Ind. Appl.*, vol. 52, no. 1, pp. 531–547, Jan./Feb. 2016.

[30] D. Thenathayalan and J. Park, “Highly flexible high-efficiency multiple-resonant wireless power transfer system using a controllable inductor,” *IEEE J. Emerg. Sel. Topics Power Electron.*, vol. 7, no. 3, pp. 1914–1930, Sep. 2019.

[31] J. W. Hsu, A. P. Hu, and A. Swain, “A wireless power pickup based on directional tuning control of magnetic amplifier,” *IEEE Trans. Ind. Electron.*, vol. 56, no. 7, pp. 2771–2781, Jul. 2009.

[32] J. Tian and A. P. Hu, “A dc-voltage-controlled variable capacitor for stabilizing the ZVS frequency of a resonant converter for wireless power transfer,” *IEEE Trans. Power Electron.*, vol. 32, no. 3, pp. 2312–2318, Mar. 2017.

[33] *Wireless Power Transfer for Light-Duty Plug-In/Electric Vehicles and Alignment Methodology*, Standard J2954_201904, 2019. [Online]. Available: http://saemobilus.sae.org/content/J2954_201904/

[34] R. Bosshard *et al.*, “Modeling and η-α-Pareto optimization of inductive power transfer coils for electric vehicles,” *IEEE J. Emerg. Sel. Topics Power Electron.*, vol. 3, no. 1, pp. 50–64, Mar. 2015.

[35] M. Budhia, J. T. Boys, G. A. Covic, and C. Huang, “Development of a single-sided flux magnetic coupler for electric vehicle IPT charging systems,” *IEEE Trans. Ind. Electron.*, vol. 60, no. 1, pp. 318–328, Jan. 2013.

[36] A. Zaheer, H. Hao, G. A. Covic, and D. Kacprzak, “Investigation of multiple decoupled coil primary pad topologies in lumped IPT systems for interoperable electric vehicle charging,” *IEEE Trans. Power Electron.*, vol. 30, no. 4, pp. 1937–1955, Apr. 2015.

[37] S. Y. Jeong, J. H. Park, G. P. Hong, and C. T. Rim, “Autotuning control system by variation of self-inductance for dynamic wireless EV charging with small air gap,” *IEEE Trans. Power Electron.*, vol. 34, no. 6, pp. 5165–5174, Jun. 2019.

[38] D. Medini and S. Ben-Yaakov, "A current-controlled variable inductor for high frequency resonant power circuits," in *Proc. IEEE Appl. Power Electron. Conf. Expo.*, Feb. 1994, pp. 219–225.

[39] J. M. Alonso, M. S. Perdiqão, D. G. Vaquero, A. J. Calleja, and E. S. Saraiva, "Analysis design experimentation on constant-frequency DC–DC resonant converters with magnetic control," *IEEE Trans. Power Electron.*, vol. 27, no. 3, pp. 1369–1382, Mar. 2012.

[40] M. S. Perdigo, J. M. Alonso, M. A. Dalla Costa, and E. S. Saraiva, "Using magnetic regulators for the optimization of universal ballasts," *IEEE Trans. Power Electron.*, vol. 23, no. 6, pp. 3126–3134, Nov. 2008.

[41] E. Rozanov and S. Ben-Yaakov, "Analysis of current-controlled inductors by new SPICE behavioral model," *HAIT J. Sci. Eng. B*, vol. 2, no. 3–n4, pp. 558–570, 2005.

[42] Y. Hu, L. Huber, and M. M. Jovanovic, "Single-stage universal-input AC/DC LED driver with current-controlled variable PFC boost inductor," *IEEE Trans. Power Electron*, vol. 27, no. 3, pp. 1579–1588, Mar. 2012.

[43] J. M. Alonso, M. Perdigão, G. Z. Abdelmessih, M. A. D. Costa, and Y. Wang, "SPICE modeling of variable inductors and its application to single inductor LED driver design," *IEEE Trans. Ind. Electron.*, vol. 64, no. 7, pp. 5894–5903, Jul. 2017.

[44] J. M. Alonso, G. Martínez, M. Perdigão, M. R. Cosetin, and R. N. Prado, "A systematic approach to modeling complex magnetic devices using SPICE: Application to variable inductors," *IEEE Trans. Power Electron.*, vol. 31, no. 11, pp. 7735–7746, Nov. 2016.

[45] S. S. Williamson, A. K. Rathore, and F. Musavi, "Industrial electronics for electric transportation: Current state-of-the-art and future challenges," *IEEE Trans. Ind. Electron.*, vol. 62, no. 5, pp. 3021–3032, May 2015.

[46] A. A. Hussein and I. Batarseh, "A review of charging algorithms for nickel and lithium battery chargers," *IEEE Trans. Veh. Technol.*, vol. 60, no. 3, pp. 830–838, Mar. 2011.

Zhuhaobo Zhang (Student Member, IEEE) received the B.S. degree in electrical engineering from Zhejiang University, Hangzhou, China, in 2017, where he is currently working toward the Ph.D. degree in electrical engineering.

His main research interests include wireless power transfer, resonant converters, and electric vehicle charging systems.

Fan Zhu received the B.S. degree in electrical engineering in 2012 from Zhejiang University, Hangzhou, China, where he is currently working toward the Ph.D. degree in electrical engineering.

His research interests include inductive power transfer systems, magnetic integration and resonant converters.

Dehong Xu (Fellow, IEEE) was born in China, in 1961. He received the B.S., M.S., and Ph.D. degrees from the Department of Electrical Engineering, Zhejiang University, Hangzhou, China, in 1983, 1986, and 1989, respectively.

Since 1996, he has been with the College of Electrical Engineering, Zhejiang University, China, as a Full Professor. He was a Visiting Scholar in the University of Tokyo, Japan, from June 1995 to May 1996. From June to December 2000, he was a Visiting Professor in CPES of Virginia Tech, USA. From February 2006 to April 2006, he was a Visiting Professor in ETH, Switzerland. His current research interests include power electronics topology and control, power conversion for energy efficiency and renewable energy. He has authored eight books and more than 200 IEEE journal or conference papers. He owns more than 40 patents.

Dr. Xu is the recipient of four IEEE journal or conference paper awards. He is an At-Large Adcom Member of the IEEE Power Electronics Society. He is Co-Editor in Chief of IEEE Open Journal of Power Electronics, an Associate Editor of the IEEE TRANSACTIONS ON POWER ELECTRONICS etc. He is the IEEE PELS Distinguish Lecturer from 2015 to 2018. In 2016, he received IEEE PELS R. D. Middlebrook Achievement Award.

Philip T. Krein (Fellow, IEEE) received the B.S. degree in electrical engineering and the A.B. degree in economics and business from Lafayette College, Easton, PA, USA, in 1978, and the M.S. and Ph.D. degrees in electrical engineering from the University of Illinois at Urbana–Champaign, Champaign, IL, USA, in 1980 and 1982, respectively.

He was an Engineer with Tektronix, Beaverton, OR, USA. He was a Senior Fulbright Scholar with the University of Surrey, Guildford, UK, from 1997 to 1998. From 2003 to 2014, he was a Founder and Director of SolarBridge Technologies, Inc., Austin, TX, USA, a developer of long-life integrated inverters for solar energy, and now part of Enphase. He holds the Grainger Endowed Chair Emeritus in electric machinery and electromechanics and is Director of the Grainger Center for Electric Machinery and Electromechanics at the University of Illinois at Urbana–Champaign. He is also Executive Dean of the Zhejiang University–University of Illinois Institute for Engineering in Haining, China. He holds 42 U.S. patents. His current research interests include all aspects of power electronics, machines, drives, electric transportation, and electrical energy, with an emphasis on nonlinear control approaches.

Dr. Krein is a Registered Professional Engineer in Illinois and Oregon. In 2003, he received the IEEE William E. Newell Award in power electronics. He is a past President of the IEEE Power Electronics Society, served as a member of the IEEE Board of Directors, and is also past Chair of the IEEE TRANSPORTATION ELECTRIFICATION COMMUNITY. He is an Associate Editor of the IEEE Open Journal of Power Electronics. He is a member of the U.S. National Academy of Engineering and a fellow of the U.S. National Academy of Inventors.

Hao Ma (Senior Member, IEEE) received the B.S., M.S., and Ph.D. degrees from Zhejiang University, Hangzhou, China, in 1991, 1994 and 1997, respectively, all in electrical engineering.

Since 1997, he has been a Lecturer, Associate Professor, and Professor at Zhejiang University. From 2007 to 2008, he was a Delta Visiting Scholar at the North Carolina State University. He is the Vice Dean of the ZJU-UIUC Institute. He has authored two books and has authored or coauthored over 200 technical papers. His current research interests include advanced control in power electronics, wireless power transfer, fault diagnosis of power electronic circuits and systems, and application of power electronics.

Dr. Ma is currently the Director of Academic Committee of China Power Supply Society. He is the Associate Editor of the IEEE Journal of Emerging and Selected Topics in Power Electronics and the Journal of Power Electronics. He was the AdCom Member of the IEEE Industrial Electronics Society, the Technical Program Chair of the IEEE ISIE 2012, IEEE PEAC 2014 and IEEE PEAC 2018.